Disclaimer

This is a problem set (as turned in) for the module physics601.

This problem set is not reviewed by a tutor. This is just what I have turned in.

All problem sets for this module can be found at
http://martin-ueding.de/de/university/msc_physics/physics601/.

[disclaimer]

Lab report

Mößbauer effect

Experiment K221 – Universität Bonn

Martin Ueding
mu@martin-ueding.de

Lino Lemmer
l2@uni-bonn.de

2016-03-02

Tutor: Peter Klassen

In this experiment we examine the γ-spectrum of ^{57}Fe. The aim is to find the Landé factors g for the ground state and the first excited state by measuring the hyperfine structure and Mößbauer spectrum respectively of the 14.4 keV transition. Line widths and the isometric shift are to be determined from the spectrum. By this a deeper understanding of recoilless emission and absorption as well of basic terms in nuclear physics should be achieved.

Contents

Permission to upload

I, Martin Ueding, would like to scan and upload this lab report with your corrections to my website martin-ueding.de. There, the original lab report as well as the reviewed one will be licensed under the "Creative Commons Attribution-ShareAlike 4.0 International License". Is that okay with you?

Yes ☐ No ☐

1. Theory

1.1. Absorption and resonances

Like the electrons in an atom, the constituents of a nucleus also have excited states and associated energy levels. As the nucleus is orders of magnitude smaller than the whole atom, the relevant energies are orders of magnitude larger. The hydrogen transition energies are in the order of 1 eV to 10 eV whereas the transition energies cobalt and iron are in the order of 10 keV to 100 keV.

If the energy matches an allowed transition, a nucleus can also absorb electromagnetic radiation and transition into an excited state. As most nuclei in a metal are in the groundstate, the highest absorption can be obtained by a transition from the groundstate. Photons with the required energy are created by an excited nucleus of the same isotope decaying into the groundstate.

The experimental setup here has a radiation source made from cobalt (^{57}Co). This decays into excited iron (^{57}Fe) via electron capture (EC), see Figure 1.1. The excited nucleus in turn will decay into the groundstate via some metastable states. See Figure 1.2 for the decay scheme of the radioactive material used in this experiment. The transition into the groundstate is the one from $j^P = 3/2^-$ to $1/2^-$ with an energy gap of $\hbar\omega_0 = 14.4\,\mathrm{keV}$.

The emission lines are not perfectly sharp. This limits the chance of absorption by the same kind of nucleus. The broadening effects are the following:

Natural width The lifetime τ of every metastable state is limited. If it were not, one would not observe the transition. Together with the energy-time-uncertainty this directly leads to a line width of

$$\Gamma = \frac{\hbar}{\tau}\,.$$

This broadening via finite lifetime leads to an Lorentzian line shape stemming from the Breit-Wigner prescription for a resonance which is a good approximation for narrow resonances.

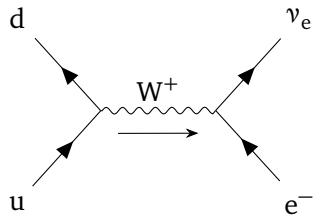

Figure 1.1.: Electron capture, leading order contribution. Time goes upwards.

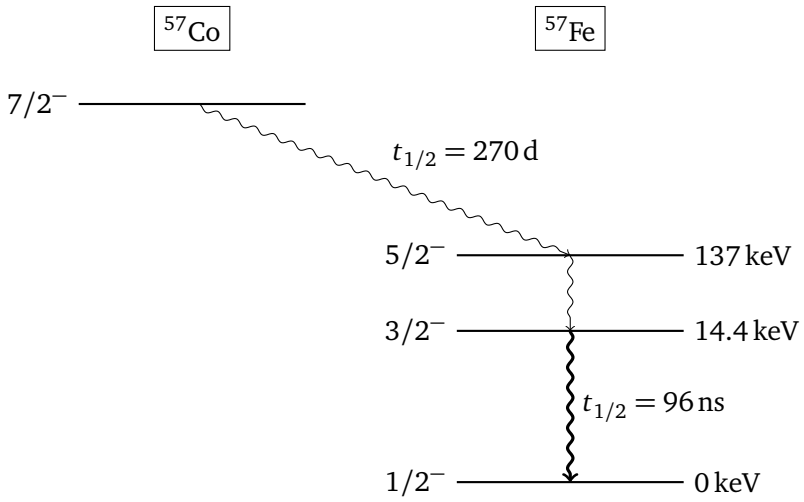

Figure 1.2.: Decay scheme of ^{57}Co into ^{57}Fe. Cobalt from the source undergoes electron capture (EC) with a very long halftime. The transition between to the groundstate (thick) is the Mößbauer energy level we are interested in. Figure adapted from Schatz, Weidinger, and Deicher [SWD10, Fig. 4.8].

Our line of interest, the 14.4 keV-line, has a lifetime of 141 ns and therefore a width of $\Gamma = 4.7 \times 10^{-9}$ eV. Compared to energy of the photons themselves, this is a relative width of 3.3×10^{-13}. That is very small compared to the other effects. [SWD10, p. 42]

Doppler effect A relative motion between source and target will lead to a Doppler shift. The Lorentz transformation connecting the two systems boosts the photon's energy. Linearizing the $\cosh(\rho)$, we obtain a boosted energy of $\hbar\omega_0(1+v/c)$. If the source particles are subject to thermal motions, the spectrum will be broadened. At room temperature, the shifts in energy are around 10×10^{-2} eV [SWD10, p. 43], depending on the angle of motion and emission. Doppler broadening leads to an Gaussian line shape.

The natural line width can be ignored when the thermal Doppler effect is present.

Recoil The photon carries momentum $\hbar k$. In the center of mass frame of the emitting nucleus, the nucleus will take the recoil $-\hbar k$. The energy of the nucleus then is $(\hbar k)^2/2M$, where M is the mass of nucleus. This energy is subtracted from the photon; the photon has a reduced frequency when emitted from a free nucleus.

Taking all those effects together, it becomes unlikely that the photons emitted by a gas of decaying cobalt will be absorbed by a gas of iron, ignoring that it might be impractical to realize this situation experimentally. The issue of the recoil can be reduced by embedding the nuclei of interest into a solid state. The lattice will absorb the excess momentum and due to its practically infinite mass (some 10^{23} larger), there will be no recoil velocity and therefore no energy shift in the photon.

1.2. Debye-Waller Factor

Although there is no energy shift caused by recoil, the energy is still shifted due to thermal motion of the atoms. Even at $T = 0\,\mathrm{K}$, there will be a shift because of zero-point energy. To get a measure of how temperature, γ-energy and mass of the lattice influence the emission, one can find the Debye-Waller factor, which is the ratio of the unshifted spectrum to the real one. For temperatures below the material specific Debye temperature Θ, the factor is given by

$$f_\mathrm{D}(T, E_\gamma, M) = \exp\left(-\frac{3E_\gamma^2}{4Mc^2 k_\mathrm{B}\Theta}\left[1 + \frac{2\pi^2}{3}\left(\frac{T}{\Theta}\right)^2\right]\right),$$

analog to the expression given by Schatz, Weidinger, and Deicher [SWD10, p. 42].

For iron, the Debye temperature is $\Theta = 470\,\mathrm{K}$ [Hun07, Tab. 6.1], so we are well below this in our experiment. Together with $E_\gamma = 14.4\,\mathrm{keV}$, the iron mass $M = 9.45 \times 10^{-26}\,\mathrm{kg}$ and assuming room temperature ($T = 292\,\mathrm{K}$), we see that the fraction has the value 0.0730, the square bracket has the value 3.54 which yields a total Debye-Waller factor of 0.772 for our experimental situation. This is high enough to give a decent signal-to-noise ratio.

1.3. Magnetic hyperfine structure

The angular momentum l and the spin s of the nucleus couple to a combined spin j. The component along the quantization axis, m_j, takes values between $-j$ and j. The various states organize themselves into the irreducible representations of SU(2), the multiplets with spin j and $(2j+1)$ states each. The different multiplets have different energies, the energies within the same multiplet are degenerate, see left part of Figure 1.3. Breaking the SU(2) symmetry of the spins give the nuclear analogue of the Zeeman effect. This is done with an external magnetic field by the interaction term $-\boldsymbol{\mu}\cdot\boldsymbol{B}$. The degeneracy is broken and each multiplet is split up into equidistant levels, see the right part of said figure.

The magnetic moment $\boldsymbol{\mu}$ is related to the spin j via the nuclear magneton μ_N or the gyromagnetic ratio γ,

$$\mu = \underbrace{g\frac{\mu_\mathrm{N}}{\hbar}}_{\gamma}\hbar j\,.$$

Choosing the quantization axis along the external magnetic field $\boldsymbol{B}$ will simplify the interaction $-\boldsymbol{\mu}\cdot\boldsymbol{B}$ to $-|\boldsymbol{B}|g\mu_\mathrm{N}m_j$. The m_j are (half-)integers and therefore equidistant. This makes the energy levels equidistant within a multiplet.

Both source and target are embedded into a solid, therefore there is little thermal fluctuation and also very little recoil. This means that the lines are rather sharp. Only the target nuclei is embedded into a magnetic field. This magnetic field comes from the magnetic domains in the ferromagnetic iron metal. The source iron nuclei do not have the Zeeman splitting and therefore always emit a pretty exact 14.4 keV line. In order for the target in the magnetic field to absorb the emitted photons, their energy needs to be adjusted.

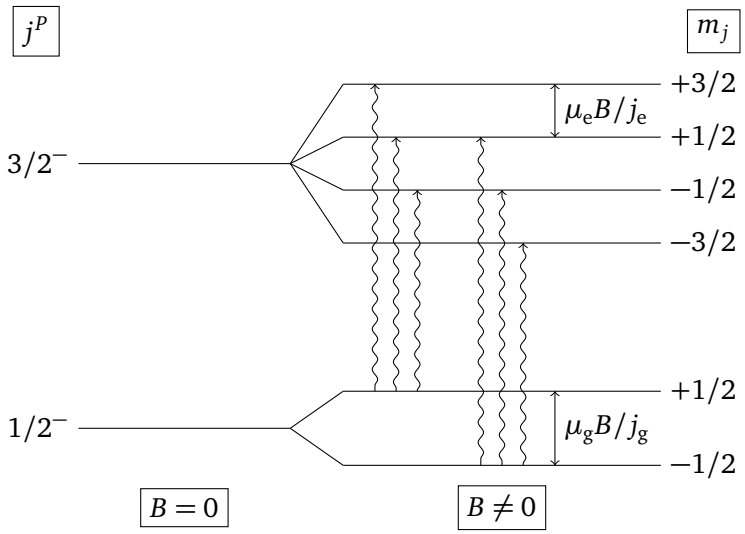

Figure 1.3.: Hyperfine structure of the 14.4 keV-M1-line in ^{57}Fe, our Mößbauer transition. Figure adapted from Schatz, Weidinger, and Deicher [SWD10, Fig. 4.22].

By moving the target with a motor, one can leverage the Doppler shift to alter the energy of the photon. As this velocity is controlled, one can effectively measure the energy shifts and therefore the hyperfine structure in the iron target. We are interested in the deviation from $\hbar\omega_0 = 14.4\,\mathrm{keV}$ and want to extract the magnetic moment of the groundstate and the exited state.

The needed relation between Doppler velocity v and the magnetic moments μ, μ' is

$$v = \frac{cB}{\hbar\omega_0}\left[\frac{\mu}{j}m_j - \frac{\mu'}{j'}m'_j\right],$$

where the primed quantities are the exited state [SWD10, (4.42)]. Expressing the magnetic moments in terms of the nuclear magneton, we see the relation between the Landé factors more clearly:

$$v = \frac{cB\mu_N}{\hbar\omega_0}\left[g m_j - g' m'_j\right]. \tag{1.1}$$

Inside the solid, the magnetic flux density is 33(1) T. All other quantities are known, the prefactor has the value $0.0237(7)\,\mathrm{m\,s^{-1}}$. As g and m_j are of the order of magnitude one, the experimental setup with $v_{\max} = 0.006\,\mathrm{m\,s^{-1}}$ will be sensible.

The selection rule for magnetic dipole (M1) radiation is $(m_j - m'_j) \in \{-1, 0, 1\}$. Therefore we expect to see six velocities with high absorption.

1.4. Isomeric shift and quadrupole moment

The iron nuclei in the source and target are embedded into a solid. This means that each nucleus is surrounded by a lot of other charged particles which create a non-constant electric field. The nucleus is not a point charge, therefore it does interact with the electric potential beyond a monopole interaction.

We assume that the electric potential that is created outside of the nucleus does not vary too much across the volume of the nucleus. Then we can expand the electric potential around the nucleus like

$$\Phi(\boldsymbol{r}) = \Phi_0 + \frac{\partial \Phi}{\partial x^i} x^i + \frac{1}{2} \frac{\partial^2 \Phi}{\partial x^i \partial x^j} x^i x^j + \mathrm{O}(x^3),$$

where we have used Einstein's summation convention [SWD10, (3.19)]. We can identify three terms:

Constant The constant term is the monopole interaction, it just gives rise to a common shift in the energies and is not relevant for our experiment as we can only observe the difference in energy levels, i.e. the photon energy.

Linear The gradient is a dipole interaction. Quantum mechanics enforces the nuclear states to be parity eigenstates, therefore the expectation value of the dipole moment is zero. The linear term does not create any shift in the energy.

Quadratic The Hessian gives rise to an electric quadrupole interaction and the isomeric shift. We will need to further analyze the Hessian.

The shift in energy by each of those terms is given by an appropriate integration against the charge density of the nucleus. For the quadratic term we have

$$E^{(2)} = \frac{1}{2} \frac{\partial^2 \Phi}{\partial x^i \partial x^j} \int \mathrm{d}^3 r \, \rho(\boldsymbol{r}) \, x^i x^j .$$

Since the Hessian is a real symmetric matrix, it can be diagonalized by an orthogonal transformation. Let the eigenvalues of the Hessian be λ_i, then we can split up the electric energy like follows into a pure-trace and a traceless term:

$$\begin{aligned} E^{(2)} &= \frac{1}{2} \sum_i \lambda_i \int \mathrm{d}^3 r \, \rho(\boldsymbol{r}) \, x_i^2 \\ &= \frac{1}{6} \sum_i \lambda_i \int \mathrm{d}^3 r \, \rho(\boldsymbol{r}) \, r^2 + \frac{1}{2} \int \mathrm{d}^3 r \, \rho(\boldsymbol{r}) \sum_i \lambda_i \left[x_i^2 - \frac{r^2}{3} \right]. \end{aligned}$$

The electric potential also obeys the Poisson equation, therefore we also have

$$\triangle \Phi = \sum_i \lambda_i = \frac{e}{\varepsilon_0} |\psi(0)|^2 ,$$

i.e. the charge density at the origin by the electron wave functions is proportional to the trace of the Hessian. The first summand in the above splitting is the isomeric term and we can rewrite it

as

$$E_{\mathrm{I}} := \frac{1}{6}\frac{e}{\varepsilon_0}|\psi(0)|^2 \int \mathrm{d}^3 r\, \rho(\boldsymbol{r})\, r^2 \,.$$

The integral over the charge density with r^2 is the second moment of the charge distribution and therefore proportional to $\langle r^2 \rangle$, the expectation value of the squared radius. The proper normalization includes $1/Ze$.

We see that the isomeric term depends on the shape of the nucleus but does not lead to any splitting depending on m_j like we saw with an external magnetic field. The energy difference can be expressed as a Doppler velocity

$$v = \frac{Ze^2c}{6\varepsilon_0\hbar\omega_0}\left(|\psi_{\mathrm{T}}(0)|^2 - |\psi_{\mathrm{S}}(0)|^2\right)\left(\langle r_{\mathrm{e}}^2\rangle - \langle r_{\mathrm{g}}^2\rangle\right),$$

as given by Schatz, Weidinger, and Deicher [SWD10, (4.31)]. If the iron nuclei in source (S) and target (T) are embedded into different crystals, then $|\psi(0)|^2$ will be different there. We also need the mean squared radius of the excited (e) and ground (g) state to differ in order for this effect to be picked up. In our experiment we will see this as a common shift independent of m_j.

The second term in the splitting is the quadrupole term. If the potential is SO(3) symmetric, all the eigenvalues λ_i are equal. The three summands will all yield the same term, the sum will be zero. Only if the potential is asymmetric, the eigenvalues will be different. Such an electric potential with a quadrupole moment will give rise to another energy splitting, the quadrupole splitting.

This expression is invariant under parity, so the splitting is only sensitive to $|m_j'|$ and we can therefore distinguish it from the magnetic splitting.

[SWD10, pp. 33, 34]

2. Experimental setup and measurement

2.1. Setup

The ^{57}Co source is located in a shielding lead box. The γ-rays escape through an opening in the target's direction. The absorber is a thin ^{57}Fe plate attached to a motor, which allows us to move it with tunable but constant velocity over a distance of 25.1(2) mm unto the source and away from it. Behind the absorber, there is a proportional detector. This setup is shown in Figure 2.1.

Its signal is fed into an amplifier and then into a single channel analyzer (SCA), c.f. Figure 2.2. After digitizing the signals, they are counted in two counters (n_{RL} and n_{LR}) depending on the direction of motion of the absorber.

The motor steering control opens the gates on the respective counters, depending on the direction of motion. Every full left-swing, the run counter N is increased by one. The motor control also takes care that a measurement starts and stop only at full left-swing. The timer gives a signal every 10 ms to another SCA, which sends the signal to the two counters t_{RL} and t_{LR}. Their gates are also controlled by the motor control.

2.2. Measurement

Before starting, we have to find the energy window for the SCA with an oscilloscope to only count 14.4 keV incidents. This also reduces noise. For that the window is opened completely. The oscilloscope is triggered with the SCA signal and shows the analog signal from the amplifier. On the screen, we can see the typical asymmetric peak shape of a proportional photon detector. With the fluorescence of screen we can see a couple lumps of peaks. The lump in the middle is the one of the line that we are interested in. The SCA window is restricted on the range of 66 to 100 and we can see that only the interesting lump of peaks is left.

After that, we start the first measurement by resetting all the counters and checking every single LED. Then we press "Start" on the motor controller. On the next full left swing of the absorber, the gates are opened and we see the counters start registering events.

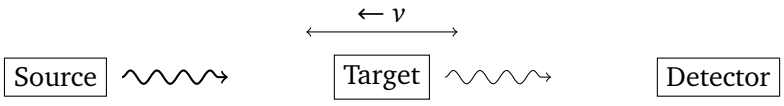

Figure 2.1.: Setup of the experiment, source emits photons which might be absorbed by the target or go through to the detector. The velocity v is defined towards the source, i.e. higher v means higher E_γ.

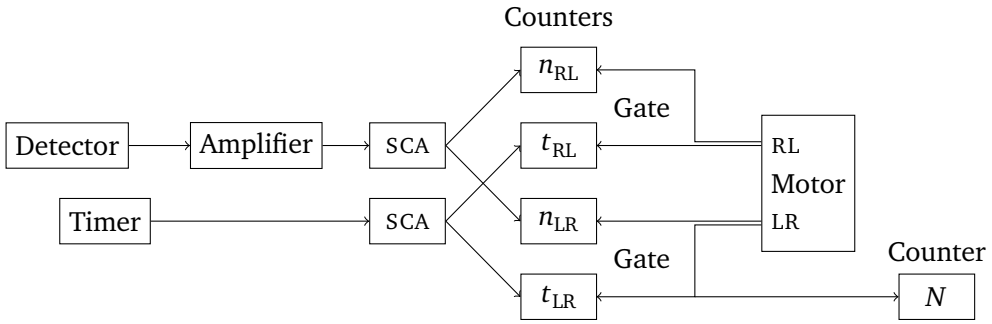

Figure 2.2.: Principal scheme of the electronic setup. The events are counted in n_{RL} and n_{LR}. The timer gives events to the time counters t_{RL} and t_{LR}. The gates of the counters are controlled by the motor control unit. Every full left-swing leads to a bump of the run counter N.

After a couple minutes, the number of events on both sides (n_{LR} and n_{RL}) are over 7000. This number was chosen as the relative uncertainty of $1/\sqrt{n}$ then is around $1/83$, which should be good enough for our purposes here. We instruct the motor controller to stop. Then at at the next full left-swing, the measurement is stopped. The number of runs N, the motor setting, the times t_{LR} and t_{RL} as well as the number of events n_{LR} and n_{RL} are read off by us. All raw measurements can be fund in the table in Appendix A.

From here, we change the motor setting by four ticks on the scale and let it run again. We repeat this procedure until the motor setting is down to 10. After that, the motor does not become slower but reverses the direction.

3. Analysis

3.1. Velocity of target

First we have to compute the actual velocity of the target. In each measurement we have N runs back and forth. The displacement for one direction (half a run) is $s = 25.1(2)\,\mathrm{mm}$. The total time spend going from left to right is t_{LR}, so we can compute the velocity with

$$v_{\mathrm{LR}} = \frac{sN}{t_{\mathrm{LR}}} \qquad \text{and} \qquad v_{\mathrm{RL}} = \frac{sN}{t_{\mathrm{RL}}}\,.$$

We were warned that the relation between the motor setting and the actual speed might not be monotonic. Therefore we have checked this, see Figure 3.1 for a graphical representation of the data. It is linear but the velocities in left–right and right–left direction are not the same. This is not a problem as we use the velocity and not the motor setting for the analysis. We lack a few data points as we could not reach small negative velocities due to this shifting.

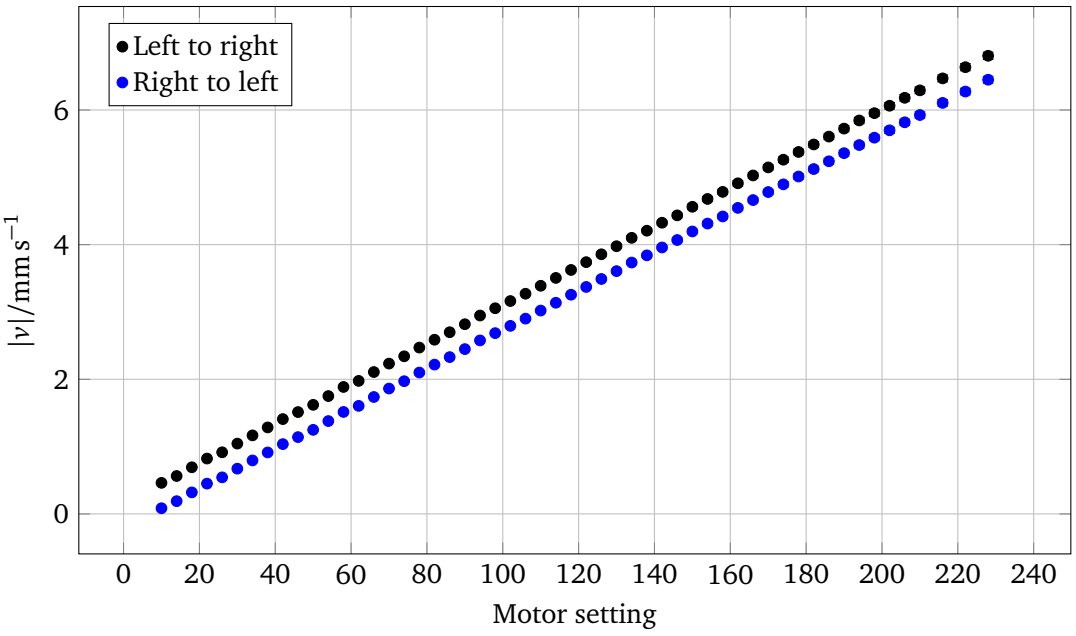

Figure 3.1.: Relation of motor setting (units on the control potentiometer) and the actual speed. The error bars are so small, that they hide behind the markers.

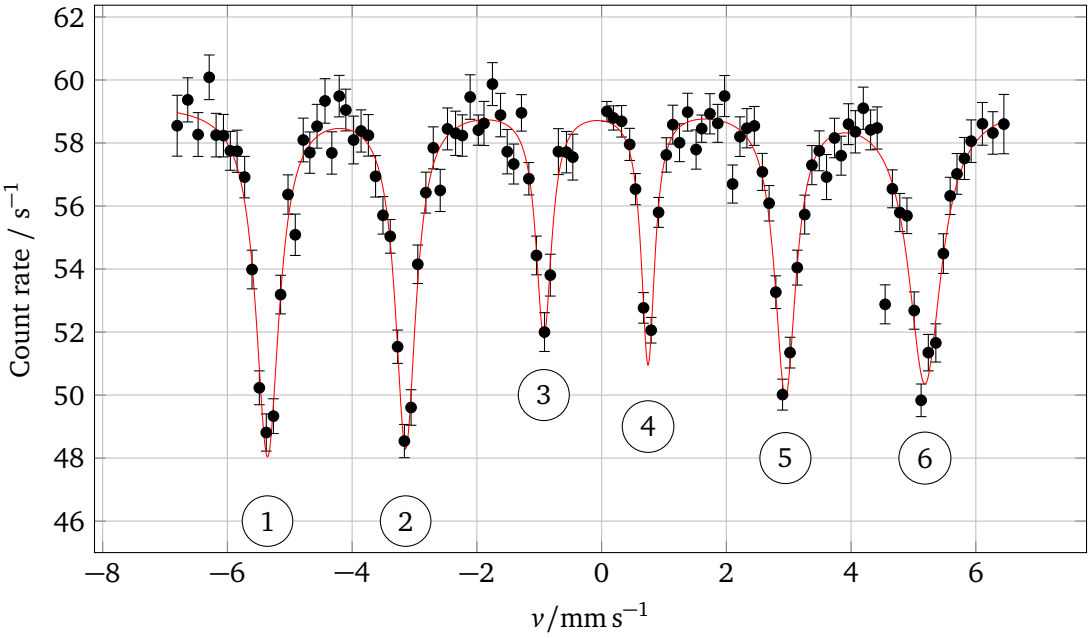

Figure 3.2.: Count rate versus velocity. Also included is a fitted sum of six Lorentzian curves and a constant offset.

3.2. Count rates

For each measurement, we compute the count rate simply with $\dot{n}_{\mathrm{LR}} = n_{\mathrm{LR}}/t_{\mathrm{LR}}$ (and similarly for right–left). The count rates versus the velocity are shown in Figure 3.2. There we can see the transmission spectrum. The background of around $60\,\mathrm{s}^{-1}$ is the transmission of the photons to the detector. We see six distinct dips in the transmission, those are the resonance frequencies. Keeping in mind that the photon energy is $\hbar\omega_0(1 + v/c)$ and $v \ll c$ in our experiment, the lines are remarkably sharp.

The dips are modeled with a Lorentzian curve, we choose the following parametrization:

$$L(x, \mu, \Gamma, I) = \frac{I}{\pi} \frac{\frac{1}{2}\Gamma}{(x-\mu)^2 + \left(\frac{1}{2}\Gamma\right)^2}.$$

We fit a sum of six Lorentzian curves and a constant offset to the data. In order to make this $6 \times 3 + 1 = 19$ parameter system stable, we carefully tune the initial parameters of the least-squares-algorithm. Table 3.3a holds our final fit parameters for the Lorentzian curves, the constant offset is $59.3(2)\,\mathrm{s}^{-1}$. The error estimates are the square roots of the diagonal of the covariance matrix and therefore likely to be too small.

3.3. Line widths

From the width Γ in $\mathrm{mm\,s}^{-1}$, which is the *full width at half maximum* (FWHM) of the Lorentzian curve, we can compute the width in energy ΔE using the Doppler effect. We had that the velocity

$\mu/\mu\mathrm{m\,s^{-1}}$	$\Gamma/\mu\mathrm{m\,s^{-1}}$	$I/\mu\mathrm{m\,s^{-2}}$
−5357(12)	451(41)	−7885(582)
−3142(11)	397(37)	−6729(514)
−927(18)	302(50)	−3433(453)
745(10)	262(40)	−3327(362)
2947(13)	409(44)	−5847(504)
5184(19)	641(61)	−8887(720)

(a) Fit parameters and errors for the Lorentz dips. We have the mean μ, the width Γ and the integral I.

$\Gamma/\mu\mathrm{m\,s^{-1}}$	$\Delta E/\mathrm{neV}$	$\delta\ /\ 10^{-13}$
451(41)	22(2)	15(1)
397(37)	19(2)	13(1)
302(50)	14(2)	10(2)
262(40)	13(2)	9(1)
409(44)	20(2)	14(1)
641(61)	31(3)	21(2)

(b) Velocity width Γ of the absorption lines, corresponding energy width and also relative line width.

Table 3.3.: Fit parameters and derived quantities.

dependent energy of the photon is given by

$$E(v) = \hbar\omega_0\left(1 + \frac{v}{c}\right).$$

Our Γ describes the width of v, so we can write

$$\Delta E = \hbar\omega_0\frac{\Gamma}{c}.$$

The relative width δ is $\Delta E/E$ and using above relations we have $\delta = \Gamma/c$. The converted widths are shown in Table 3.3b.

The relative line widths are in the order of 10^{-12}. Compared to the natural line width of 3.3×10^{-13} this is only a factor of three to four larger!

3.4. Isomeric shift

Assuming that we the energy splitting is symmetric (as it definitely is for the magnetic splitting), the spectrum must be symmetric around $v = 0$. However, if we have an isomeric shift, the whole spectrum will be shifted to some v_0 and the spectrum is symmetric around that velocity.

Taking a simple average of the velocities of all dips, we will obtain v_0. Using the six values that we have, we get $v_0 = -0.09(1)\,\mathrm{mm\,s^{-1}}$. This corresponds do an energy shift of $-4.4(7)\,\mathrm{neV}$.

3.5. Landé factors

From the six lines that we have, we can also compute the Landé factor g for the ground state ($j = 1/2^-$) and g' for the excited state ($j = 3/2^-$). First we must determine which line belongs to which transition. We number the lines with increasing energy according to Figure 3.2.

The distance between transitions with either m_j or m_j' fixed must be equal, anticipating a negligible quadrupole splitting. Therefore there are only two possibilities:

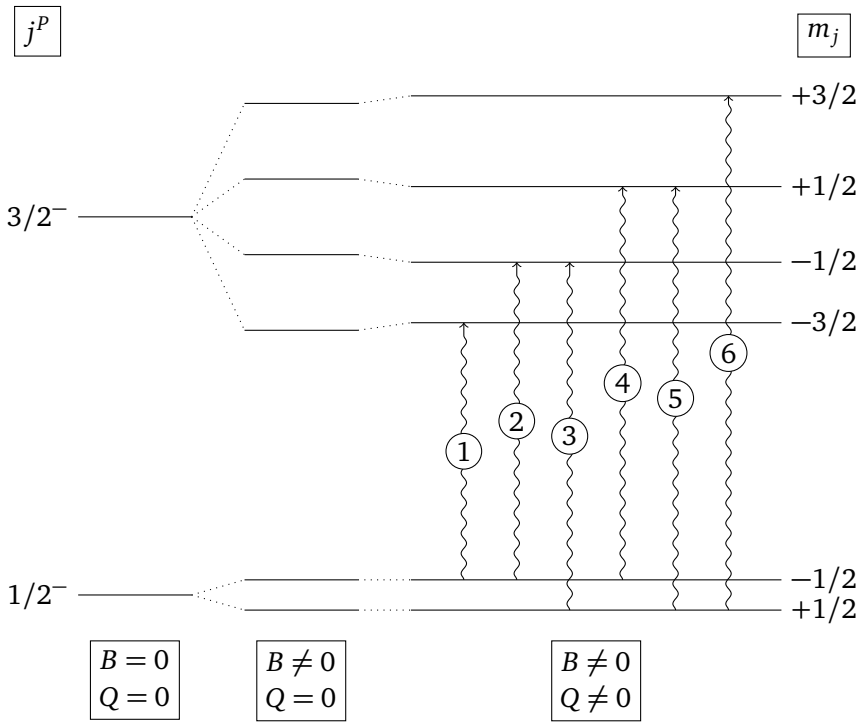

Figure 3.4.: Transition lines with no splitting (left), purely magnetic splitting (center) and magnetic and quadrupole splitting (right). Our six transitions from the spectrum are ordered by energy. Note that the m_j for the groundstate are switched as the sign of g differs from the sign of g'.

1. The splitting in the ground state is large. Therefore we expect to see two narrow triplets which are displaced by more than their intermediate spacing. Lines 1, 2 and 3 correspond to the three lines coming from $m_j = +1/2$ and lines 4, 5, and 6 correspond to the three transitions starting from $m_j = -1/2$.
2. The splitting in the excited state is large. Therefore we expect two wide triplets which are just slightly shifted against each other. Another way would be to interpret this as a triplet where each line is slightly split up again. Then lines 1, 3 and 5 come from $m_j = +1/2$ and 2, 4 and 6 come from $m_j = -1/2$.

Option 1 seems to be the obvious choice from Figure 3.2. We have tried this, but we do not get reasonable results for g and g' this way. Looking at the literature values for Landé factors, it seems we must expect $|g'| > |g|$. Therefore option 2 is the actual phenomenon. Looking at the intensities of the absorption lines, option 2 seems to be more likely as adjacent pairs have roughly the same intensity. Figure 3.4 shows the energy levels and our six transitions.

We therefore average over the following velocity differences to obtain the ground state energy splitting: $(\nu_3 - \nu_2)$ and $(\nu_5 - \nu_4)$. For the excited state, we take $(\nu_4 - \nu_2)$, and $(\nu_5 - \nu_3)$. In principle, the differences $(\nu_2 - \nu_1)$ and $(\nu_6 - \nu_5)$ are also suitable if we assume that we do not have any quadrupole splitting. As we want to compute the quadrupole splitting as well, we may only use the former two differences. Those only have $m'_j = \pm 1/2$ and are therefore unaffected by quadrupole splitting.

From this we obtain the averaged velocities

$$\Delta v = 2.209(7)\,\mathrm{mm\,s^{-1}}, \qquad \Delta v' = -3.88(1)\,\mathrm{mm\,s^{-1}}.$$

The negative sign in $\Delta v'$ comes from the negative sign in Equation (1.1). Dividing by $cB\mu_N/\hbar\omega_0$, we obtain the Landé factors

$$g = 0.101(3), \qquad g' = -0.178(5).$$

The uncertainty in g and g' includes the uncertainty in the magnetic as this was given by $B = 33(1)\,\mathrm{T}$.

3.6. Quadrupole shift

The quadrupole shift is the difference in $|m_j'| = 3/2$ and $|m_j'| = 1/2$ states. In order to compute the shift, we use

$$\Delta\nu_Q = \frac{(\nu_6 - \nu_5) - (\nu_2 - \nu_1)}{2}.$$

The first summand is the difference between the $m_j' = +3/2$ and $+1/2$ lines. The second summand is the difference between the $-1/2$ and $-3/2$ line. If we do not have any quadrupole splitting, both would be equal (within uncertainty), the quadrupole shift would be zero.

The numerical value that we obtain is $\Delta\nu_Q = 0.012(15)\,\mathrm{mm\,s^{-1}}$, which is indeed zero well within our uncertainty. Therefore can conclude that there is vanishing quadrupole distortion of the electric field around the iron nucleus.

4. Conclusion

In the measured spectrum, we resolved the fine structure of ^{57}Fe due to its own ferromagnetic field inside the metal. The widths of the resonances are only a factor of four larger than natural line width; an astonishing feat for a tabletop experiment at room temperature!

We were able to determine the Landé factors for the $j^P = 1/2^-$ and $j^P = 3/2^-$ levels in ^{57}Fe to be

$$g = 0.101(3), \qquad g' = -0.178(5).$$

Our values should be compared to the literature values

$$g_{\text{lit}} = 0.090\,604(9), \qquad g'_{\text{lit}} = -0.155\,31(4),$$

taken from Schatz, Weidinger, and Deicher [SWD10, Fig. 4.8]. The literature value is too many standard errors away from our measurements. Therefore we must have underestimated our errors. Otherwise the values are in the right ballpark.

The isomeric shift from the source to target material is $v_0 = -4.4(7)\,\text{neV}$. Qualitatively, this effect comes from the different environment the ^{57}Fe nuclei are exposed to in source and target material. We know that the mean square radius of the groundstate and excited state are different each in both materials and that the electron density at the nucleus is also different in both materials.

We determined that there is vanishing quadrupole splitting in the iron absorber. This is probably due to the symmetry of the iron lattice and that the iron metal is a conductor.

A. Raw measurements

All our raw measurements are in the following table.

N	Motor	$t_{\mathrm{LR}}/10\,\mathrm{ms}$	n_{LR}	$t_{\mathrm{RL}}/10\,\mathrm{ms}$	n_{RL}
17	228	6270	3671	6616	3877
32	222	12 104	7186	12 802	7466
31	216	12 027	7008	12 744	7469
30	210	11 968	7191	12 708	7378
30	206	12 182	7096	12 944	7444
31	202	12 833	7473	13 655	7786
36	198	15 179	8766	16 168	9106
30	194	12 884	7439	13 742	7488
30	190	13 156	7488	14 051	7258
32	186	14 330	7736	15 333	7873
38	182	17 380	8730	18 618	9278
30	178	14 005	6836	15 024	7915
34	174	16 219	8001	17 432	9708
29	170	14 142	7522	15 224	8494
29	166	14 477	8160	15 612	8828
25	162	12 776	7038	13 803	7299
23	158	12 068	7011	13 065	7640
25	154	13 412	7738	14 549	8499
22	150	12 103	7084	13 160	7778
21	146	11 885	7052	12 955	7560
22	142	12 766	7364	13 951	8175
23	138	13 722	8163	15 030	8657
22	134	13 464	7950	14 787	8600
16	130	10 099	5867	11 135	6338
20	126	13 016	7599	14 384	8307
20	122	13 423	7818	14 889	8531
19	118	13 159	7493	14 646	8162
22	114	15 751	8774	17 604	9514
26	110	19 256	10 598	21 602	11 092
24	106	18 417	9491	20 766	10 386
22	102	17 462	8476	19 767	10 529
19	98	15 609	7743	17 758	9960
17	94	14 478	7840	16 555	9450
15	90	13 361	7539	15 377	9002
14	86	13 019	7531	15 085	8820
13	82	12 610	7124	14 711	8562
13	78	13 205	7718	15 535	8808

N	Motor	$t_{LR}/10\,ms$	n_{LR}	$t_{RL}/10\,ms$	n_{RL}
11	74	11 791	6875	14 004	8331
12	70	13 488	7855	16 171	9480
10	66	11 909	7081	14 450	8515
20	62	25 402	14 837	31 275	18 282
9	58	11 977	7021	14 912	8618
9	54	12 903	7725	16 377	9659
8	50	12 390	7296	16 075	9325
7	46	11 612	6703	15 397	9020
8	42	14 252	8171	19 361	11 156
9	38	17 579	10 364	24 734	13 801
10	34	21 512	12 233	31 584	16 442
6	30	14 420	7849	22 402	11 821
5	26	13 706	7127	23 095	13 057
4	22	12 205	6567	22 305	12 927
3	18	10 865	6272	23 514	13 800
3	14	13 360	7710	39 685	23 333
2	10	10 872	6257	59 282	34 978

You can also view this data at https://github.com/martin-ueding/physics601-reports/blob/master/K221_Moessbauer/Data/runs.tsv and download it at https://raw.githubusercontent.com/martin-ueding/physics601-reports/master/K221_Moessbauer/Data/runs.tsv.

Bibliography

[Hun07] Siegfried Hunklinger. *Festkörperphysik*. Oldenbourg, 2007. ISBN: 987-3-486-57562-0.

[SWD10] Günter Schatz, Alois Weidinger, and Manfred Deicher. *Nukleare Festkörderphysik*. 4. Vieweg + Teubner, 2010. ISBN: 978-3-8351-0228-6.